

Cold three-body recombination in helium-helium-silver-atom collisions using the hybrid slow-variable-discretization–adiabatic hyperspherical R -matrix approach

Hiroya Suno ^{*}

Research Center for Computing and Multimedia Studies, Hosei University, 3-7-2 Kajino-cho,
Koganei-shi, Tokyo 184-8584, Japan

 (Received 20 November 2023; revised 16 March 2024; accepted 25 March 2024; published 11 April 2024)

We study three-body recombination in the helium-helium-silver system at cold collision energies. The three-body Schrödinger equation is solved combining the slow variable discretization and adiabatic approaches with the R -matrix propagation method, in order to calculate the product-state-selective total and partial recombination rates in the ${}^4\text{He} + {}^4\text{He} + \text{Ag}$ system. Recombination at collision energies less than 10 mK is found to take place dominantly to the product molecule ${}^4\text{He Ag}$ in its least bound state, while the three atoms recombine mainly to the ${}^4\text{He}_2$ molecule in its ground state at higher collision energies.

DOI: [10.1103/PhysRevA.109.042814](https://doi.org/10.1103/PhysRevA.109.042814)

I. INTRODUCTION

Three-body recombination, a process in which three free particles collide to form a two-body bound state and a free particle enabling the dissipation of the energy, is one of the most fundamental and ubiquitous chemical reactions. The three-body recombination processes are relevant for a wide variety of systems in physics and chemistry. In cold and ultracold systems, three-body recombination impacts the lifetime and stability of ultracold dilute gases [1–8] and plays an important role in the formation and trapping of cold and ultracold molecules [9–13]. It is also shown in Refs. [14–20] that the three-body recombination processes provide an efficient way to investigate the formation of van der Waals molecules in helium buffer-gas-cooled magnetic traps.

From the theoretical viewpoint, quantitative calculations of recombination for realistic atomic three-body systems are limited by the number of diatomic bound states existing in such systems. Most of the available calculations for recombination for realistic systems have been confined to those possessing just a few two-body bound states, namely, the $\text{He} + \text{He} + \text{He}$ [21,22], $\text{He} + \text{He} + \text{alkali-metal}$ [19], and $\text{H} + \text{H} + \text{alkali-metal}$ [20] systems, and even these were challenging calculations. In fact, when using the adiabatic hyperspherical representation, the existence of many two-body bound states leads to a complex set of sharp nonadiabatic avoided crossings in the hyperspherical potential curves at short distances, and in particular, for nonzero total angular momenta, $J > 0$, states. The large number of sharp avoided crossing creates numerical difficulties for the adiabatic representation, which is formulated with d/dR couplings.

There are known to us two promising ways to overcome these difficulties: one is the “diabatic-by-sectors” (DBS) method proposed by Parker *et al.* [23], and the other the slow variable discretization (SVD) method, proposed by Tolstikhin *et al.* [24]. The SVD method, which we adopt in this

work, has been used and applied successfully to three-body bound-state calculations [25,26] and three-body $\text{H} + \text{Ne-Ne}$ collisions. Although the latter calculations did not require numerical solution of the hyperradial equation out to large distances, it is crucial to solve it out to very large distances when studying ultracold three-body recombination processes, which makes application of SVD demanding in terms of memory and CPU time. Wang *et al.* [27] developed a methodology within the hyperspherical adiabatic representation that allows for the treatment of systems with many two-body bound states, separating the hyperradial domain into two regions, and applying the SVD method at short distances, where many avoided crossings appear, and using the adiabatic method at large distances, where adiabatic potential curves are smooth. This methodology was applied successfully to nonrotational $J = 0$ systems of three identical bosons interacting through two-body potential models adjusted to support eight to ten two-body bound states.

The purpose of this work is to test the above-mentioned methodology proposed by Wang *et al.* [27], extending it to nonrotational and rotational, $J \geq 0$, $\text{He} + \text{He} + \text{Ag}$ systems. The ${}^4\text{He} + {}^4\text{He} + \text{Ag}$ system possesses five two-body bound states in total— ${}^4\text{He Ag}$ s -, p -, d -, f -wave bound states and ${}^4\text{He}_2$ s -wave bound state—not so many, but enough to see a complex set of sharp avoided crossings in the adiabatic hyperspherical potential curves, particularly for nonzero total angular momenta. The ${}^4\text{He} + {}^4\text{He} + \text{Ag}$ recombination rate calculations are an interesting extension of the previous investigations in Ref. [19] that dealt with the ${}^4\text{He} + {}^4\text{He} + \text{alkali-metal}$ atomic recombination, including here a coinage atom, silver, in recombination calculations. All these calculations are relevant to helium buffer-gas cooling experiments, in which the weakly bound van der Waals molecules HeAg [15] and HeLi [17] were produced by three-body recombination. By using the above-described hybrid SVD-adiabatic hyperspherical R -matrix propagation approach, we compute the product-state-selective three-body recombination rates as functions of the collision energy. We treat not only zero total angular momentum, $J = 0$, states, but also $J > 0$ states,

*hiroya.suno.73@hosei.ac.jp

so that recombination beyond the ultracold regime can be considered.

The organization of this paper is as follows: Sec. II presents the theoretical approach; the results are presented in Sec. III; we finally conclude and summarize in Sec. IV.

II. METHOD

The main ideas of the hybrid SVD-adiabatic hyperspherical R -matrix propagation approach are described in Ref. [27] for the specific case of three identical bosons in the $J = 0$ symmetry. We present here the approach emphasizing the modifications necessary when three particles are not identical and that they are in $J > 0$ states.

After separating out the center-of-mass motion, the triatomic system can be described using modified Smith-Whitten hyperspherical coordinates $(R, \Omega) \equiv (R, \theta, \varphi, \alpha, \beta, \gamma)$ [21,28–31]. The hyperradius R characterizes the overall size of the system, while the two hyperangles θ and φ describe the internal motion of the three-body system. α, β , and γ are the usual Euler angles. By rescaling the usual wave function Ψ_i as $\psi_i = R^{5/2}\Psi_i$, the three-body Schrödinger equation in hyperspherical coordinates [in atomic units (a.u.)] is given by

$$\left[-\frac{1}{2\mu} \frac{\partial^2}{\partial R^2} + \frac{\Lambda^2 + 15/4}{2\mu R^2} + V(R, \theta, \varphi) \right] \psi_i(R, \Omega) = E \psi_i(R, \Omega), \quad (1)$$

where

$$\Lambda^2 = -\frac{4}{\sin 2\theta} \frac{\partial}{\partial \theta} \sin 2\theta \frac{\partial}{\partial \theta} + \frac{4}{\sin^2 \theta} \left(i \frac{\partial}{\partial \varphi} - \cos \theta \frac{J_z}{2} \right)^2 + \frac{2J_x^2}{1 - \sin \theta} + \frac{2J_y^2}{1 + \sin \theta} + J_z^2 \quad (2)$$

is the squared grand angular-momentum operator, (J_x, J_y, J_z) the body-fixed frame (x, y, z) components of the total angular momentum \mathbf{J} , and $\mu = \sqrt{m_1 m_2 m_3 / (m_1 + m_2 + m_3)}$ with m_1, m_2 , and m_3 being the masses of the three atoms. The dependence on the Euler angles drops out for the $J = 0$ symmetry. In Eq. (1), $V(R, \theta, \varphi)$ is the total potential energy that will be given in Eq. (36). For $J > 0$, the squared grand angular-momentum operator in Eq. (2) causes a difficulty since it contains several singularities due to its denominators which become zero at $\theta = 0$ and/or at $\theta = \pi/2$. These singularities, collectively referred to as ‘‘Eckart singularities,’’ are characteristics of all instantaneous principal axes systems. A proper treatment of the Eckart singularities was proposed by Kendrick *et al.* [31] using a hybrid discrete-variable representation-finite-basis-representation (DVR-FBR) approach. Since we adopt simple basis splines in θ without any boundary conditions for the sake of simplicity, in this work, we must be careful in dealing with wave functions localized around the regions $\theta = 0$ (corresponding to an oblate symmetric top geometry) and $\theta = \pi/2$ (corresponding to a linear configuration).

In our three-body problem, the good quantum numbers are the total angular momentum J , its projection M , and the inversion parity Π , so that the Schrödinger equation (1)

can be solved separately for each fixed set of J and Π . The key ingredients in our numerical approach are the hyperspherical adiabatic potentials and channel functions, which are defined as solutions of the adiabatic eigenvalue problem

$$\left[\frac{\Lambda^2}{2\mu R^2} + \frac{15}{8\mu R^2} + V(R, \theta, \varphi) \right] \Phi_v(R; \Omega) = U_v(R) \Phi_v(R; \Omega). \quad (3)$$

This adiabatic equation is solved by expanding the channel function on the normalized Wigner functions $\tilde{D}_{KM}^J(\alpha, \beta, \gamma) = [(2J + 1)/8\pi]^{1/2} D_{KM}^J(\alpha, \beta, \gamma)$:

$$\Phi_v^{JM\Pi}(R; \Omega) = \sum_K \phi_{Kv}^{J\Pi}(R; \theta, \varphi) \tilde{D}_{KM}^J(\alpha, \beta, \gamma), \quad (4)$$

where K , denoting the projection of \mathbf{J} on a body-fixed axis, takes on the integer values that satisfy $-J \leq K \leq J$ and $\Pi = (-1)^K$. For a system containing two identical bosons ($m_2 = m_3$) for which the wave function is symmetric under exchange, the permutation symmetry can be taken into account via the boundary conditions:

$$(-1)^{J+K} \phi_{-Kv}^{J\Pi}(R; \theta, 0) = \phi_{Kv}^{J\Pi}(R; \theta, 0), \quad (5)$$

$$(-1)^{J+K+1} \left. \frac{\partial \phi_{-Kv}^{J\Pi}}{\partial \varphi} \right|_{\varphi=0} = \left. \frac{\partial \phi_{Kv}^{J\Pi}}{\partial \varphi} \right|_{\varphi=0}, \quad (6)$$

$$(-1)^J \phi_{-Kv}^{J\Pi}(R; \theta, \pi) = \phi_{Kv}^{J\Pi}(R; \theta, \pi), \quad (7)$$

$$(-1)^{J+1} \left. \frac{\partial \phi_{-Kv}^{J\Pi}}{\partial \varphi} \right|_{\varphi=\pi} = \left. \frac{\partial \phi_{Kv}^{J\Pi}}{\partial \varphi} \right|_{\varphi=\pi}, \quad (8)$$

and the hyperangle φ , originally defined in the range $[0, 2\pi]$, is now restricted to $[0, \pi]$. These boundary conditions differ from those in the case of three identical bosons, in which the hyperangle φ is restricted to $[0, \pi/3]$. The $\phi_{Kv}^{J\Pi}(R; \theta, \varphi)$ in Eq. (4) is expanded on a direct product of fifth-order basis splines [32] in $\theta \in [0, \pi/2]$ and $\varphi \in [0, \pi]$.

Our goal is to determine, from the solutions of Eq. (1), the scattering matrix $\underline{\mathcal{S}}$. To accomplish this goal, the R matrix ($\underline{\mathcal{R}}$) must be computed first, which is the quantity that can be used subsequently to determine the scattering matrix, see Eqs. (32) and (33). The R matrix is defined as

$$\underline{\mathcal{R}}(R) = \underline{F}(R) [\underline{\tilde{F}}(R)]^{-1}, \quad (9)$$

where matrices \underline{F} and $\underline{\tilde{F}}$ are given in terms of the solutions of Eqs. (1) and (3) by

$$F_{vi}(R) = \int d\Omega \Phi_v(R; \Omega)^* \psi_i(R, \Omega), \quad (10)$$

$$\tilde{F}_{vi}(R) = \int d\Omega \Phi_v(R; \Omega)^* \frac{\partial}{\partial R} \psi_i(R, \Omega). \quad (11)$$

The R -matrix propagation method [33] propagates the solutions of Eq. (1) from a small hyperradius $R = a$ to a large hyperradius $R = b$. The range a to b is divided up into a number of subranges and the R -matrix is propagated across each of these in turn. Let us consider the subrange with left boundary

a_1 and right boundary a_2 ($>a_1$), within which the Schrödinger equation (1) must be solved. One important ingredient in solving the Schrödinger equation within this subrange is the use of the discrete variable representation (DVR) [34,35]. Our DVR basis function $\pi_l(R)$ are defined from the L -point Gauss-Lobatto quadrature points x_l and weights w_l ($l = 1, 2, \dots, L$) [36] defined over the interval $x \in [-1, 1]$. By scaling these quadrature points and weights as $R_l = (a_2 - a_1)x_l/2 + (a_2 + a_1)/2$ and $\omega_l = (a_2 - a_1)w_l/2$, the integrals of any function $g(R)$ can be approximated over an arbitrary interval $R \in [a_1, a_2]$ by

$$\int_{a_1}^{a_2} g(R) dR \approx \sum_{l=1}^L g(R_l) \omega_l. \quad (12)$$

The DVR basis functions are constructed as

$$\pi_l(R) = \frac{1}{\sqrt{\omega_l}} \prod_{l' \neq l} \frac{R - R_{l'}}{R_l - R_{l'}}, \quad (13)$$

which have the important property $\pi_l(R_{l'}) = \delta_{ll'}/\sqrt{\omega_l}$.

At small hyperradii, where there exists numerous sharp avoided crossings, we employ the SVD approach, which consists in developing the total wave function as

$$\psi_i(R, \Omega) = \sum_{lv} c_{lv,i} \pi_l(R) \Phi_v(R_l; \Omega). \quad (14)$$

On the other hand, at large hyperradii, where the nonadiabatic couplings are smooth functions of R , the adiabatic approach is used, expanding the total wave function as

$$\psi_i(R, \Omega) = \sum_{lv} c_{lv,i} \pi_l(R) \Phi_v(R; \Omega). \quad (15)$$

In both the SVD and adiabatic approaches, the hyperradial wave functions $F_{vi}(R)$ at DVR points R_l are easily found from the coefficients $c_{lv,i}$, using

$$F_{vi}(R_l) = \omega_l^{-1/2} c_{lv,i}. \quad (16)$$

Insertion of Eq. (14) or (15) into the Schrödinger Eq. (1) yields the equation for the expansion coefficients $c_{lv,i}$:

$$[\underline{\mathcal{H}} - E \underline{1}] \underline{\vec{c}}_i = \underline{\mathcal{L}} \underline{\vec{c}}_i, \quad (17)$$

where $\underline{1}$ is the identity matrix.

In the SVD approach based on the expansion (14), the matrix elements of $\underline{\mathcal{H}}$ and $\underline{\mathcal{L}}$ are given by

$$\begin{aligned} \mathcal{H}_{lv,l'v'} &= \frac{1}{2\mu} \left[\int_{a_1}^{a_2} dR \pi_l'(R) \pi_{l'}(R) \right] \mathcal{O}_{lv,l'v'} \\ &+ U_v(R_l) \delta_{ll'} \delta_{vv'}, \end{aligned} \quad (18)$$

$$\mathcal{L}_{lv,l'v'} = \frac{1}{2\mu} [\pi_l(R) \pi_{l'}'(R)] \Big|_{a_1}^{a_2} \mathcal{O}_{lv,l'v'}, \quad (19)$$

where

$$\mathcal{O}_{lv,l'v'} = \int d\Omega \Phi_v(R_l; \Omega)^* \Phi_{v'}(R_{l'}; \Omega) \quad (20)$$

are the overlap matrix elements between different adiabatic channels defined at different hyperradial DVR points. On the

other hand, in the adiabatic approach based on the expansion (15), the $\underline{\mathcal{H}}$ and $\underline{\mathcal{L}}$ matrices are expressed as

$$\begin{aligned} \mathcal{H}_{lv,l'v'} &= \frac{1}{2\mu} \int_{a_1}^{a_2} dR \pi_l'(R) \pi_{l'}(R) \delta_{vv'} \\ &+ \left[U_v(R_l) \delta_{vv'} + \frac{P_{vv'}^2(R_l)}{2\mu} \right] \delta_{ll'} - \frac{1}{2\mu} \int_{a_1}^{a_2} \\ &\times dR [\pi_l(R) P_{vv'}(R) \pi_{l'}'(R) - \pi_{l'}'(R) P_{vv'}(R) \pi_l(R)], \end{aligned} \quad (21)$$

$$\mathcal{L}_{lv,l'v'} = \frac{1}{2\mu} [\pi_l(R) \delta_{vv'} \pi_{l'}'(R) + \pi_l(R) P_{vv'}(R) \pi_{l'}(R)] \Big|_{a_1}^{a_2}. \quad (22)$$

Here, the nonadiabatic couplings matrix elements are defined and expressed by

$$P_{vv'}(R) = \int d\Omega \Phi_v(R; \Omega)^* \frac{\partial}{\partial R} \Phi_{v'}(R; \Omega), \quad (23)$$

$$\begin{aligned} Q_{vv'}(R) &= \int d\Omega \Phi_v(R; \Omega)^* \frac{\partial^2}{\partial R^2} \Phi_{v'}(R; \Omega) \\ &= P_{vv'}^2(R) + P'_{vv'}(R), \end{aligned} \quad (24)$$

and these are evaluated numerically by a simple differencing scheme:

$$\frac{\partial}{\partial R} \Phi_{v'}(R; \Omega) \approx \frac{\Phi_{v'}(R + \Delta R; \Omega) - \Phi_{v'}(R - \Delta R; \Omega)}{2\Delta R}. \quad (25)$$

By diagonalizing $\underline{\mathcal{H}}$ over the hyperradial subrange $[a_1, a_2]$ such as $\vec{x}_n^T \underline{\mathcal{H}} \vec{x}_n = \varepsilon_n \delta_{nn'}$, and using the completeness relation $\sum_n \vec{x}_n \vec{x}_n^T = \underline{1}$, Eq. (17) is rewritten as

$$\vec{c}_i = [\underline{\mathcal{H}} - E]^{-1} \underline{\mathcal{L}} \vec{c}_i = \sum_n \frac{\vec{x}_n \vec{x}_n^T}{\varepsilon_n - E} \underline{\mathcal{L}} \vec{c}_i. \quad (26)$$

From here, we introduce the matrices

$$(\underline{\mathcal{R}}_{11})_{vv'} = \frac{1}{\omega_1} \sum_n \frac{x_{1v,n} x_{1v',n}}{2\mu(\varepsilon_n - E)}, \quad (27)$$

$$(\underline{\mathcal{R}}_{12})_{vv'} = \frac{1}{\sqrt{\omega_1 \omega_L}} \sum_n \frac{x_{1v,n} x_{Lv',n}}{2\mu(\varepsilon_n - E)}, \quad (28)$$

$$(\underline{\mathcal{R}}_{21})_{vv'} = \frac{1}{\sqrt{\omega_1 \omega_L}} \sum_n \frac{x_{Lv,n} x_{1v',n}}{2\mu(\varepsilon_n - E)}, \quad (29)$$

$$(\underline{\mathcal{R}}_{22})_{vv'} = \frac{1}{\omega_L} \sum_n \frac{x_{Lv,n} x_{Lv',n}}{2\mu(\varepsilon_n - E)}, \quad (30)$$

where, by writing $(\underline{\mathcal{R}}_{pp'})_{vv'}$, the indices p (p') stands for the left boundary ($=1$) or the right boundary ($=2$), v (v') for the numbers labeling the adiabatic potential curves. By substituting the matrix elements of $\underline{\mathcal{L}}$ from Eq. (19) or (22), inserting the definition of the R matrix at a_1 and a_2 from Eqs. (9), (10), and (11) into Eq. (25), and after some manipulation, we obtain the R -matrix propagation from the left boundary a_1 to the right boundary a_2 :

$$\underline{\mathcal{R}}(a_2) = \underline{\mathcal{R}}_{22} - \underline{\mathcal{R}}_{21} [\underline{\mathcal{R}}_{11} + \underline{\mathcal{R}}(a_1)]^{-1} \underline{\mathcal{R}}_{12}. \quad (31)$$

Once we obtain the R matrix at sufficiently large distances, the physical scattering matrix $\underline{\mathcal{S}}$ and the reaction matrix $\underline{\mathcal{K}}$ can be determined by imposing boundary conditions:

$$\underline{\mathcal{K}} = (\underline{f} - \underline{f}'\underline{\mathcal{R}})(\underline{g} - \underline{g}'\underline{\mathcal{R}})^{-1}, \quad (32)$$

$$\underline{\mathcal{S}} = (\underline{1} + i\underline{\mathcal{K}})(\underline{1} - i\underline{\mathcal{K}})^{-1}, \quad (33)$$

where \underline{f} , \underline{g} , \underline{f}' , and \underline{g}' are diagonal matrices whose elements are the energy-normalized asymptotic solutions f_v , g_v and their derivatives f'_v , g'_v , respectively. f_v and g_v are expressed in terms of spherical Bessel functions as $f_v(R) = (2\mu k_v/\pi)^{1/2} R j_{l_v}(k_v R)$ and $g_v(R) = (2\mu k_v/\pi)^{1/2} R n_{l_v}(k_v R)$, with k_v and l_v being determined by the asymptotic behavior of the potential curves in Eqs. (39) and (40). The product-state-selective three-body recombination rate is then given by

$$K_3 = \sum_{J,\Pi} K_3^{J\Pi} = \sum_{J,\Pi} \sum_{f,i} \frac{64\pi^2(2J+1)}{\mu k^4} |S_{fi}^{J\Pi}|^2, \quad (34)$$

where $k = \sqrt{2\mu E}$ is the hyperradial wave number in the incident channels and $S_{fi}^{J\Pi}$ the appropriate scattering matrix elements. The index i runs over all the incident channels, while f runs over the recombination channels relevant to the chosen product state. By designating as $K_3^{(F)}$ the total recombination rate to the product state F , the branching ratio into the product state is finally obtained by

$$r_3^{(F)} = \frac{K_3^{(F)}}{\sum_F K_3^{(F)}}. \quad (35)$$

In the SVD approach, the potential curves $U_v(R_l)$ in Eq. (3) and the overlap matrix elements \mathcal{O}_{l_v,l'_v} in Eq. (20) are calculated at every hyperradial point R_l from 10 to 600 a.u., on the grid of 60–70 hyperradial subranges each divided by an $L = 10$ -point Gauss-Lobatto quadrature. At large distances $R \gtrsim 600$ a.u., the adiabatic approach is applied. Here, the potential curves $U_v(R_l)$, the P and Q matrices in Eqs. (23) and (24) are calculated on a sparse hyperradial grid up to about 1200 a.u. These are interpolated with cubic or Akima splines on a more or less dense grid at $600 \lesssim R \lesssim 1200$ a.u., and extrapolated in an inverse polynomial series [37] from $R \approx 1200$ up to very large distances, 2×10^5 a.u., with the typical hyperradial subrange length being 15 to 30 a.u. For example, at collision energies $E \approx 10^{-5}$ K, the R matrix, including more than 30 adiabatic channels, needs to be propagated from the hyperradii $R \approx 10$ to 2×10^5 a.u. for optimal three-body recombination calculations.

The total potential energy $V(R, \theta, \varphi)$ in Eq. (1) is represented as the addition of three pair interaction potentials:

$$V(R, \theta, \varphi) = v_{\text{HeAg}}(r_{12}) + v_{\text{HeHe}}(r_{23}) + v_{\text{HeAg}}(r_{31}), \quad (36)$$

where r_{ij} are the interatomic distances, expressed in our coordinate system as

$$r_{ij} = 2^{-1/2} d_{ij} R [1 + \sin \theta \cos(\varphi + \varphi_{ij})]^{1/2}, \quad (37)$$

with $\varphi_{12} = 2 \tan^{-1}(m_2/\mu)$, $\varphi_{23} = 0$, $\varphi_{31} = -2 \tan^{-1}(m_3/\mu)$, and the d_{ij} coefficients are given by

$$d_{ij} = \left[\frac{m_k(m_i + m_j)}{\mu(m_1 + m_2 + m_3)} \right]^{1/2}, \quad (38)$$

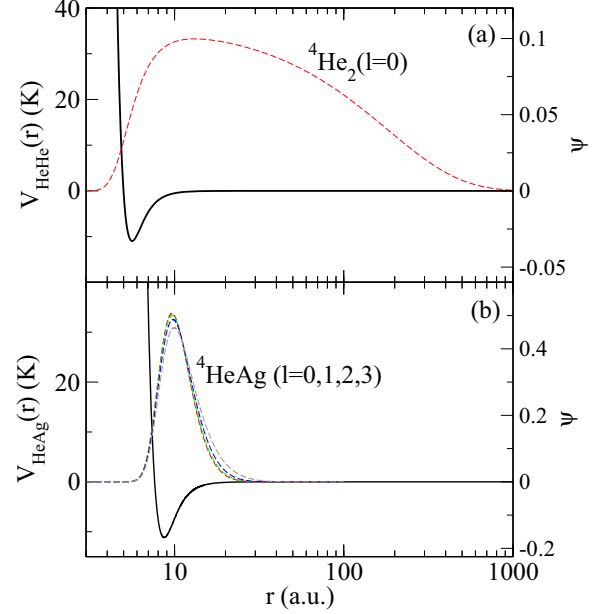


FIG. 1. (a) Helium dimer potential $v_{\text{HeHe}}(r)$ and ${}^4\text{He}_2(l=0)$ bound-state wave function. (b) Helium-silver potential $v_{\text{HeAg}}(r)$ and ${}^4\text{He Ag}(l=0, 1, 2, 3)$ bound-state wave functions.

with (i, j, k) being a cyclic permutation of $(1, 2, 3)$. The masses used are $m({}^4\text{He}) = 7298.2993$ and $m(\text{Ag}) = 194923.06$ a.u. For the helium dimer potential $v_{\text{HeHe}}(r)$, we use the probably most widely used LM2M2 representation developed by Aziz and Slaman [38], and for the helium-silver potential $v_{\text{HeAg}}(r)$, the analytical form proposed by Xie *et al.* in Ref. [39], obtained by fitting the best He-Ag potential data of Gardner *et al.* [40]. These potentials are known to support one ${}^4\text{He}_2$ zero angular momentum $l=0$ bound state and four ${}^4\text{He Ag}$ zero and nonzero angular momentum ($l=0, 1, 2, 3$) bound states. The potentials and the supported bound-state wave functions are shown together in Fig. 1. These two potentials, $v_{\text{HeHe}}(r)$ and $v_{\text{HeAg}}(r)$, do not appear to be so different from each other and are characterized by similarly short ranges and similar depths, but the ${}^4\text{He}_2(l=0)$ wave function differs surprisingly from the ${}^4\text{He Ag}(l=0, 1, 2, 3)$ wave functions, with its tail extending to about one thousand atomic units. This long-range nature of the ${}^4\text{He}_2$ wave function is, as is well known, due to the vicinity of its energy level to the two-body breakup threshold, leading to a very large s -wave scattering length. In Table I, we summarize the ${}^4\text{He}_2$ and ${}^4\text{He Ag}$ bound-state energy levels

TABLE I. ${}^4\text{He}_2$ and ${}^4\text{He Ag}$ bound-state energy levels E_2 (given in a.u. and kelvin) and the relevant s -wave scattering lengths (given in a.u. and Å).

	l	E_2 (K)	E_2 (a.u.)	a (Å)	a (a.u.)
${}^4\text{He } {}^4\text{He}$	0	-1.310×10^{-3}	-4.148×10^{-9}	100	189
${}^4\text{He Ag}$	0	-3.248	-1.028×10^{-5}	0.33	0.17
	1	-2.805	-0.883×10^{-6}		
	2	-1.938	-6.136×10^{-6}		
	3	-0.691	-2.188×10^{-6}		

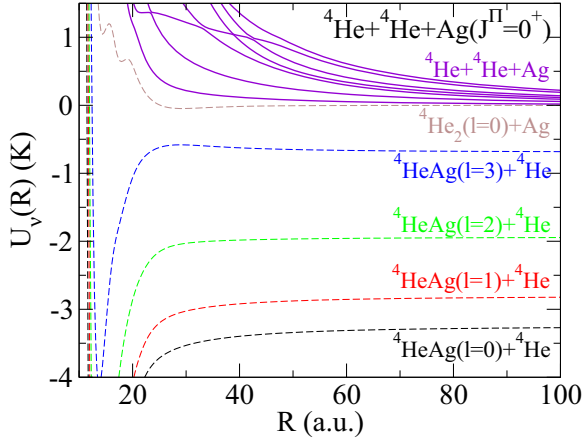


FIG. 2. The lowest adiabatic hyperspherical potential curves $U_v(R)$ ($v = 1, 2, \dots, 12$) as functions of the hyperradius R for ${}^4\text{He} + {}^4\text{He} + \text{Ag}$ in the $J^\Pi = 0^+$ symmetry. The dashed curves denote the recombination channels, and the solid curves the entrance channels.

(given in a.u. and Kelvin) and the relevant s -wave scattering lengths (given in a.u. and \AA).

III. RESULTS

Since ${}^4\text{He}_2$ and ${}^4\text{HeAg}$ possess respectively one $l = 0$ bound state and four $l = 0, 1, 2$ and 3 bound states, three-body recombination is allowed to all the five product states, ${}^4\text{HeAg}(l = 0, 1, 2, 3) + {}^4\text{He}$ and ${}^4\text{He}_2(l = 0) + \text{Ag}$, for the parity-favored cases $\Pi = (-1)^J$. However, for the parity-unfavored cases, $\Pi = (-1)^{J+1}$, by symmetry requirements, recombination is restricted to the three product states, ${}^4\text{HeAg}(l = 1, 2, 3) + {}^4\text{He}$, and is prohibited to the two other product states, ${}^4\text{HeAg}(l = 0) + {}^4\text{He}$ and ${}^4\text{He}_2(l = 0) + \text{Ag}$. Three-body recombination from the parity-unfavored cases is found to take place only at collision energies $E \gtrsim 0.1$ K, and the recombination rates are negligible at collision energies below about 0.1 K. We performed recombination rate calculations for total angular momenta up to $J = 6$ and $\Pi = \pm 1$, seemingly enough partial waves to obtain converged total recombination rates at $E \lesssim 0.2$ K.

We show here only the $J^\Pi = 0^+$ and 1^- adiabatic hyperspherical potential curves as functions of the hyperradius R , which are presented respectively in Figs. 2 and 3, but for the other symmetries, they are seen to possess similar features. The dashed curves in these figures denote the recombination channels, i.e., the final-state channels of the recombination process, corresponding to one of the possible product states, where two of the three atoms are bound with the third atom far away. The effective hyperradial potentials, defined as $W_v(R) \equiv U_v(R) - Q_{vv}(R)/(2\mu)$, for these channels possess asymptotic behavior given by

$$W_f(R) \stackrel{R \rightarrow \infty}{\approx} \frac{l_f(l_f + 1)}{2\mu R^2} + E_2^F, \quad (39)$$

where E_2^F is the bound-state energy level of the product molecule $F = {}^4\text{HeAg}$ ($l = 0, 1, 2, 3$) or ${}^4\text{He}_2(l = 0)$, and l_f the corresponding angular momentum of the third atom

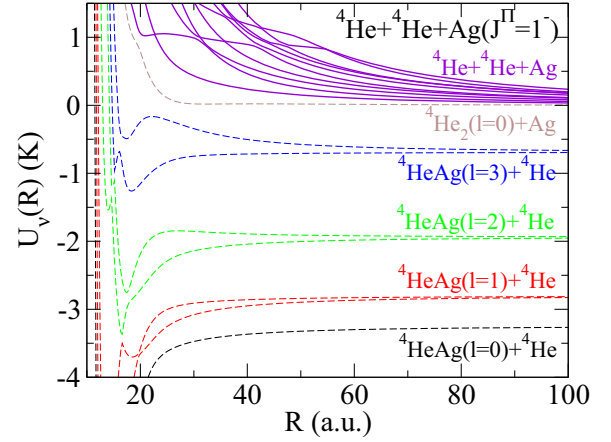


FIG. 3. The lowest adiabatic hyperspherical potential curves $U_v(R)$ ($v = 1, 2, \dots, 18$) as functions of the hyperradius R for ${}^4\text{He} + {}^4\text{He} + \text{Ag}$ in the $J^\Pi = 1^-$ symmetry.

relative to the product molecule. In Figs. 2 and 3, the solid curves denote the three-body continuum channels, i.e., the entrance channels, whose asymptotic behavior is described by

$$W_i(R) \stackrel{R \rightarrow \infty}{\approx} \frac{\lambda_i(\lambda_i + 4) + 15/4}{2\mu R^2}, \quad (40)$$

where $\lambda_i(\lambda_i + 4)$ is the eigenvalue of the grand angular-momentum operator Λ^2 [Eq. (2)]. λ_i can take on any integer value, but its possible values are restricted by symmetry requirements.

Seen from Figs. 2 and 3, the characteristic short-distance sharp avoided crossings appear only at the collision energies a little above 1 K for $J^\Pi = 0^+$, but they appear at all the energy range shown here for $J^\Pi = 1^-$ and are expected to become more complicated for the higher total angular-momentum states. All these sharp avoided crossings are known to produce numerical difficulties when applying the traditional adiabatic hyperspherical approach.

The product-state-selective total and partial ${}^4\text{He} + {}^4\text{He} + \text{Ag}$ recombination rates, K_3 and $K_3^{J^\Pi}$, as functions of the collision energy E , are presented in Fig. 4. In Fig. 4(a), where the recombination rates for the process ${}^4\text{He} + {}^4\text{He} + \text{Ag} \rightarrow {}^4\text{HeAg}(l = 0) + {}^4\text{He}$ are shown, the partial recombination rates at the lower collision energies are seen to behave as $K_3^{J^\Pi} \propto E^{\lambda_{\min}}$, where λ_{\min} is the minimum number of λ_i in Eq. (40) allowed by symmetry requirements, as is predicted by a generalized Wigner threshold law [41]. For the parity-favored cases, i.e., $J^\Pi = 0^+, 1^-, 2^+, 3^-, \dots$, we have $\lambda_{\min} = 0, 1, 2, 3, \dots$, and the low-energy partial rates are dominant in the order $0^+, 1^-, 2^+, 3^-, \dots$. This trend is also seen to apply for the partial recombination rates leading to the other three product molecules ${}^4\text{HeAg}(l = 1)$, ${}^4\text{HeAg}(l = 2)$, and ${}^4\text{HeAg}(l = 3)$, as are shown in Figs. 4(b)–4(d), respectively. The partial recombination rates for the process ${}^4\text{He} + {}^4\text{He} + \text{Ag} \rightarrow {}^4\text{He}_2(l = 0) + \text{Ag}$ in Fig. 4(e) differ significantly from those to those other product states. Here, the $J \geq 2$ partial recombination rates increase quickly with the collision energies $E \gtrsim 10^{-4}$ K, compete with the 0^+ and 1^- partial rates, and even these collision energies less than 10^{-4} K appear to be outside the

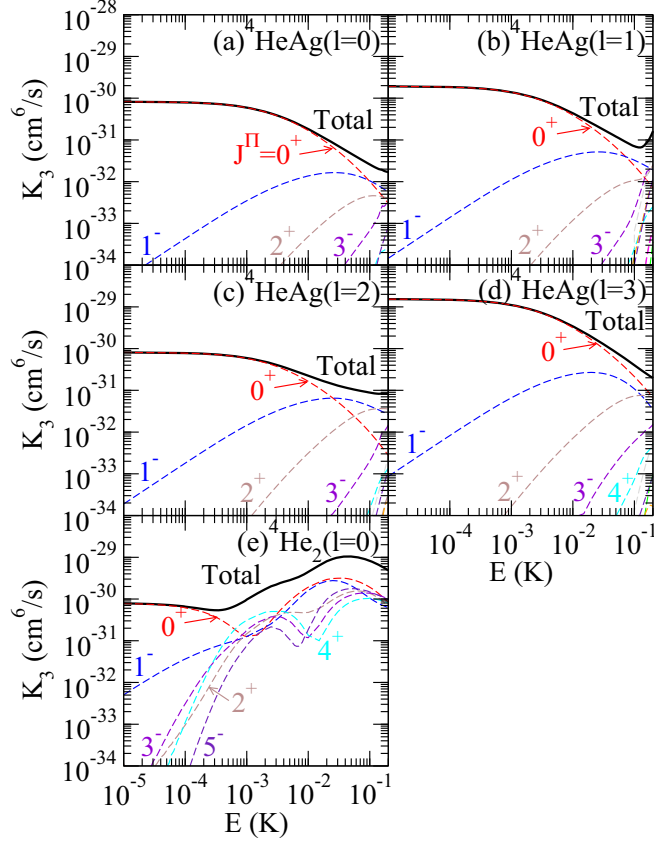


FIG. 4. Product-state-selective total and partial ${}^4\text{He} + {}^4\text{He} + \text{Ag}$ recombination rates, K_3 and $K_3^{J^\pi}$, as functions of the collision energy E to the final states (a) ${}^4\text{HeAg}(l=0) + {}^4\text{He}$, (b) ${}^4\text{HeAg}(l=1) + {}^4\text{He}$, (c) ${}^4\text{HeAg}(l=2) + {}^4\text{He}$, (d) ${}^4\text{HeAg}(l=3) + {}^4\text{He}$, and (e) ${}^4\text{He}_2(l=0) + \text{Ag}$. The solid curves denote the total rates, and the dashed curves the partial rates labeled J^π .

threshold regime. The Wigner threshold law for the ${}^4\text{He}_2 + \text{Ag}$ recombination channel is found to hold in different collision energies for the ${}^4\text{HeAg} + {}^4\text{He}$ recombination channels, which can be explained by the very large extent of the ${}^4\text{He} + {}^4\text{He}$ wave function. In Fig. 4(e), we can observe, in the $J^\pi = 0^+$ rate to ${}^4\text{He}_2(l=0)$, a Stückelberg minimum due to the destructive interference of two pathways, which is a characteristic of the 0^+ recombination to a weakly bound diatomic molecule with the scattering length being large and positive [1,21]. This minimum occurs indeed, since the ${}^4\text{He}_2$ molecule is weakly bound, and possesses a large positive scattering length, see Table I. In contrast, we do not see any such Stückelberg minimum, at least in the considered energy range, in the 0^+ recombination rates to the different rotational states of ${}^4\text{HeAg}$ presented in Figs. 4(a)–4(d), since ${}^4\text{HeAg}$ is not so weakly bound and possesses a positive but very small scattering length, as is given in Table I.

In Fig. 5(a), we compare the total ${}^4\text{He} + {}^4\text{He} + \text{Ag}$ recombination rates to the different product states, as functions of the collision energy E . We observe that, at low collision energies, the recombination rate to ${}^4\text{HeAg}(l=3) + {}^4\text{He}$ dominates over those to the other product states. However, the rate to ${}^4\text{He}_2(l=0) + \text{Ag}$ is seen to increase from $E \gtrsim 10^{-3}$ K, and become dominant over those to the other product states

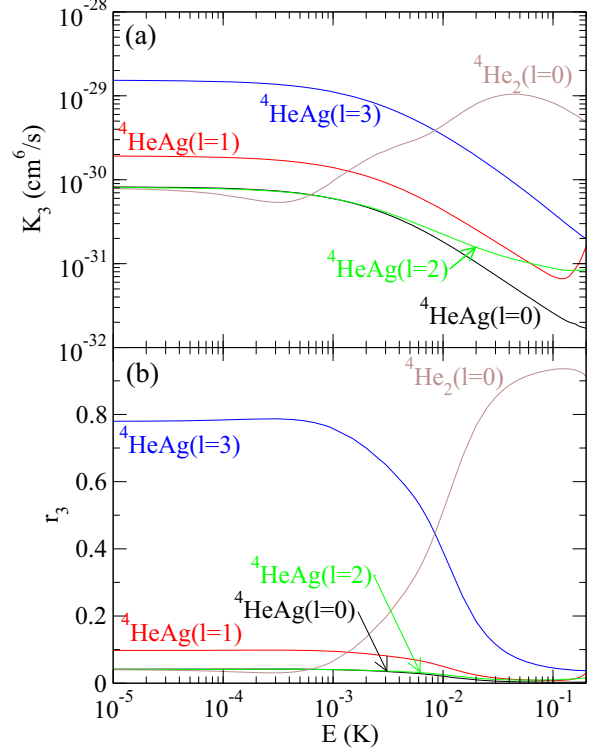


FIG. 5. (a) Product-state-selective total three-body recombination rates K_3 as functions of the collision energy E for the processes ${}^4\text{He} + {}^4\text{He} + \text{Ag} \rightarrow {}^4\text{HeAg}(l=0, 1, 2, 3) + {}^4\text{He}$ and ${}^4\text{He} + {}^4\text{He} + \text{Ag} \rightarrow {}^4\text{He}_2(l=0) + \text{Ag}$. (b) Branching ratio of the three-body recombination rates in panel (a) as functions of the collision energy E .

at $E \gtrsim 10^{-2}$ K. The branching ratios obtained from these product-state-selective total three-body recombination rates are shown in Fig. 5(b). We can see again that the branching ratio to ${}^4\text{HeAg}(l=3) + {}^4\text{He}$ dominates at $E \lesssim 10^{-2}$ K, while, at $E \gtrsim 10^{-2}$ K, recombination takes place mainly to ${}^4\text{He}_2(l=0) + \text{Ag}$. This trend can be explained in terms of the $J^\pi = 0^+$ hyperspherical adiabatic potential curves and nonadiabatic couplings. Figure 6 illustrates qualitatively the physical picture of the ${}^4\text{HeAg}(l=3)$ and ${}^4\text{He}_2(l=0)$ recombination processes dominant at low and high collision energies E . In Fig. 6, from bottom to top, the three $J^\pi = 0^+$ hyperspherical potential curves associated with the ${}^4\text{HeAg}(l=3) + {}^4\text{He}$, ${}^4\text{He}_2 + \text{Ag}$ recombination channels, and the lowest three-body ${}^4\text{He} + {}^4\text{He} + \text{Ag}$ entrance channel are depicted as functions of the hyperradius R . The gray box at small hyperradii indicates the region where the nonadiabatic couplings maximize, namely, the nonadiabatic transition region. The blue dashed and brown dash-dotted lines denote the recombination pathways dominant at low collision energies and at high collision energies, respectively. At any positive energy, the three particles are asymptotically free as $R \rightarrow \infty$. At low collision energies E , once the system tunnels inward under the three-body ${}^4\text{He} + {}^4\text{He} + \text{Ag}$ channel barrier, it can hardly recombine to the ${}^4\text{He}_2 + \text{Ag}$ potential curve since the latter channel possesses a repulsive barrier and makes the nonadiabatic transition region energetically less accessible. Instead, the system can easily recombine to the ${}^4\text{HeAg}(l=3) + {}^4\text{He}$

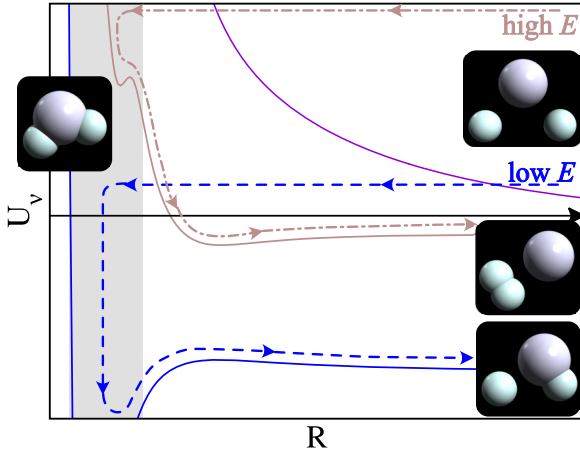


FIG. 6. Schematic three $J^\pi = 0^+$ hyperspherical potential curves associated with the ${}^4\text{He Ag}(l=3) + {}^4\text{He}$, ${}^4\text{He}_2 + \text{Ag}$ recombination channels, and three-body ${}^4\text{He} + {}^4\text{He} + \text{Ag}$ entrance channel from bottom to top (solid blue, solid brown, and solid violet curves respectively). The gray box indicates the hyperradial nonadiabatic transition region. The blue dashed and brown dash-dotted lines denote respectively the recombination pathways dominant at lower collision energies and at higher collision energies, respectively.

potential curve due to its attractive nature that makes the transition region energetically accessible, as is indicated as the blue dashed line in Fig. 6. This interplay between the repulsive or attractive potential curves and the nonadiabatic couplings can explain qualitatively why the recombination to ${}^4\text{He Ag}(l=3)$ is favored over that to ${}^4\text{He}_2(l=0)$ at low energies. At high collision energies, in contrast, both of the two recombination channels can access energetically the nonadiabatic transition region, but the system can recombine preferably to the ${}^4\text{He}_2(l=0) + \text{Ag}$ potential curve, as indicated as the brown dash-dotted line in Fig. 6, since the latter channel is the closest to the entrance channel.

Table II presents the total three-body recombination rates at the zero-energy limit, together with those for the ${}^4\text{He} + {}^4\text{He} + {}^7\text{Li}$ and ${}^4\text{He} + {}^4\text{He} + {}^{23}\text{Na}$ systems taken from Ref. [19]. The product-state-selective zero-energy total recombination rates for the ${}^4\text{He} + {}^4\text{He} + \text{Ag}$ system are found to be dominant in the order ${}^4\text{He Ag}(l=3)$, ${}^4\text{He Ag}(l=1)$, ${}^4\text{He}_2(l=0)$, ${}^4\text{He Ag}(l=0)$, and ${}^4\text{He Ag}(l=2)$. Obviously, this finding does not appear to agree with the expectation that, in ultracold three-body recombination processes, the production rate of a molecule generally decrease with its binding energy [42]. Therefore, the reason for this dependence of the production rate on the binding energy and the physics governing it remain unclear but can be explained in terms of the adiabatic potential curves and nonadiabatic couplings, as discussed so far. When comparing with the ${}^4\text{He} + {}^4\text{He} + {}^7\text{Li}$ and ${}^4\text{He} + {}^4\text{He} + {}^{23}\text{Na}$ recombination rates, the ${}^4\text{He} + {}^4\text{He} + \text{Ag}$ recombination rates are found to be surprisingly small, and two or three orders of magnitude smaller, and the relatively

TABLE II. Total three-body recombination rates at the zero-energy limit for the ${}^4\text{He} + {}^4\text{He} + X$ systems with $X = \text{Ag}$, ${}^7\text{Li}$, and ${}^{23}\text{Na}$. The rates for $X = \text{Ag}$ are obtained in the present work, and those for $X = {}^7\text{Li}$ and ${}^{23}\text{Na}$ are taken from Ref. [19].

Initial state	Final state	$K_3(E \rightarrow 0)$ (cm^6/s)
${}^4\text{He} + {}^4\text{He} + \text{Ag}$	${}^4\text{He Ag}(l=0) + {}^4\text{He}$	8.3×10^{-31}
	${}^4\text{He Ag}(l=1) + {}^4\text{He}$	1.9×10^{-30}
	${}^4\text{He Ag}(l=2) + {}^4\text{He}$	8.2×10^{-31}
	${}^4\text{He Ag}(l=3) + {}^4\text{He}$	1.6×10^{-29}
	${}^4\text{He}_2(l=0) + \text{Ag}$	8.7×10^{-31}
${}^4\text{He} + {}^4\text{He} + {}^7\text{Li}$	${}^4\text{He } {}^7\text{Li}(l=0) + {}^4\text{He}$	5.1×10^{-28}
	${}^4\text{He}_2(l=0) + {}^7\text{Li}$	2.2×10^{-28}
${}^4\text{He} + {}^4\text{He} + {}^{23}\text{Na}$	${}^4\text{He } {}^{23}\text{Na}(l=0) + {}^4\text{He}$	2.3×10^{-29}
	${}^4\text{He}_2(l=0) + {}^{23}\text{Na}$	2.3×10^{-29}

tightly bound nature of the helium-silver interaction might be playing a role in these suppressed ${}^4\text{He} + {}^4\text{He} + \text{Ag}$ recombination processes.

IV. SUMMARY

In this work, we have studied three-body recombination in ${}^4\text{He} + {}^4\text{He} + \text{Ag}$ collisions at energies below 200 mK. We have successfully calculated the product-state-selective partial and total recombination rates up to the $J^\pi = 6^\pm$ symmetries, by applying the hybrid SVD-adiabatic hyperspherical R -matrix propagation approach. At collision energies below $E \lesssim 100$ mK, the partial rates to the product molecules ${}^4\text{He Ag}(l=0, 1, 2, 3)$ behave as predicted by the generalized Wigner threshold law, while the $J \geq 1$ partial rates to ${}^4\text{He}_2(l=0)$ increase much more rapidly and appear to be outside the threshold regime even at fairly low collision energies $E \approx 0.1$ mK. At $E \lesssim 10$ mK, three-body recombination takes place dominantly to the ${}^4\text{He Ag}(l=3)$ product molecule, but at $E \gtrsim 10$ mK, the three atoms recombine preferably to ${}^4\text{He}_2(l=0)$ product molecule. Extensions of the present calculations to higher collision energies and to the ${}^3\text{He} + {}^3\text{He} + \text{Ag}$ system are also interesting subjects of study, but several technical difficulties are likely to arise due to the rapidly increasing number of contributing partial waves at higher collision energies.

ACKNOWLEDGMENTS

The author thanks H. Ueda, M. N. Hasnine, and N. Ohno for computational support. The computations were carried out using Laboratory System at Research Center for Computing and Multimedia Studies, Hosei University. The author thanks the Center for Cooperative Work on Data science and Computational science, University of Hyogo for the use of the facilities. Part of the computation was performed using Research Center for Computational Science, Okazaki, Japan (Project: 23-IMS-C225).

[1] B. D. Esry, C. H. Greene, and J. P. Burke Jr, *Phys. Rev. Lett.* **83**, 1751 (1999).

[2] J. Weiner, V. S. Bagnato, S. Zilio, and P. S. Julienne, *Rev. Mod. Phys.* **71**, 1 (1999).

- [3] P. F. Bedaque, E. Braaten, and H.-W. Hammer, *Phys. Rev. Lett.* **85**, 908 (2000).
- [4] H. Suno, B. D. Esry, and C. H. Greene, *Phys. Rev. Lett.* **90**, 053202 (2003).
- [5] H. Suno, B. D. Esry, and C. H. Greene, *New J. Phys.* **5**, 53 (2003).
- [6] T. Weber, J. Herbig, M. Mark, H.-C. Nägerl, and R. Grimm, *Phys. Rev. Lett.* **91**, 123201 (2003).
- [7] M. Schmidt, H.-W. Hammer, and L. Platter, *Phys. Rev. A* **101**, 062702 (2020).
- [8] C. H. Greene, P. Giannakeas, and J. Pérez-Ríos, *Rev. Mod. Phys.* **89**, 035006 (2017).
- [9] T. Köhler, K. Góral, and P. S. Julienne, *Rev. Mod. Phys.* **78**, 1311 (2006).
- [10] D. Blume, *Rep. Prog. Phys.* **75**, 046401 (2012).
- [11] J. Pérez-Ríos and C. H. Greene, *J. Chem. Phys.* **143**, 041105 (2015).
- [12] A. Krüchow, A. Mohammadi, A. Härter, J. H. Denschlag, J. Pérez-Ríos, and C. H. Greene, *Phys. Rev. Lett.* **116**, 193201 (2016).
- [13] A. Mohammadi, A. Krüchow, A. Mahdian, M. Deiß, J. Pérez-Ríos, H. da Silva Jr, M. Raoult, O. Dulieu, and J. Hecker Denschlag, *Phys. Rev. Res.* **3**, 013196 (2021).
- [14] N. Brahms, B. Newman, C. Johnson, T. Greytak, D. Kleppner, and J. Doyle, *Phys. Rev. Lett.* **101**, 103002 (2008).
- [15] N. Brahms, T. V. Tscherbul, P. Zhang, J. Klos, H. R. Sadeghpour, A. Dalgarno, J. M. Doyle, and T. G. Walker, *Phys. Rev. Lett.* **105**, 033001 (2010).
- [16] N. Brahms, T. V. Tscherbul, P. Zhang, J. Klos, R. C. Forrey, Y. S. Au, H. Sadeghpour, A. Dalgarno, J. M. Doyle, and T. G. Walker, *Phys. Chem. Chem. Phys.* **13**, 19125 (2011).
- [17] N. Tariq, N. A. Taisan, V. Singh, and J. D. Weinstein, *Phys. Rev. Lett.* **110**, 153201 (2013).
- [18] N. Quiros, N. Tariq, T. V. Tscherbul, J. Klos, and J. D. Weinstein, *Phys. Rev. Lett.* **118**, 213401 (2017).
- [19] H. Suno and B. D. Esry, *Phys. Rev. A* **80**, 062702 (2009).
- [20] Y. Wang, J. P. D’Incao, and B. D. Esry, *Phys. Rev. A* **83**, 032703 (2011).
- [21] H. Suno, B. D. Esry, C. H. Greene, and J. P. Burke Jr, *Phys. Rev. A* **65**, 042725 (2002).
- [22] H. Suno and B. D. Esry, *Phys. Rev. A* **78**, 062701 (2008).
- [23] G. A. Parker, R. B. Walker, B. K. Kendrick, and R. T Pack, *J. Chem. Phys.* **117**, 6083 (2002).
- [24] O. I. Tolstikhin, S. Watanabe, and M. Matsuzawa, *J. Phys. B: At., Mol. Opt. Phys.* **29**, L389 (1996).
- [25] H. Suno, *J. Chem. Phys.* **134**, 064318 (2011).
- [26] J. Wang and C. H. Greene, *Phys. Rev. A* **82**, 022506 (2010).
- [27] J. Wang, J. P. D’Incao, and C. H. Greene, *Phys. Rev. A* **84**, 052721 (2011).
- [28] R. C. Whitten and F. T. Smith, *J. Math. Phys.* **9**, 1103 (1968).
- [29] B. Johnson, *J. Chem. Phys.* **73**, 5051 (1980).
- [30] B. Lepetit and A. Kuppermann, *Chem. Phys. Lett.* **166**, 581 (1990).
- [31] B. K. Kendrick, R. T. Pack, R. B. Walker, and E. F. Hayes, *J. Chem. Phys.* **110**, 6673 (1999).
- [32] C. de Boor, *A Practical Guide to Splines; Rev. Ed.*, Applied Mathematical Sciences (Springer, Berlin, 2001).
- [33] K. Baluja, P. Burke, and L. Morgan, *Comput. Phys. Commun.* **27**, 299 (1982).
- [34] J. Lill, G. Parker, and J. Light, *Chem. Phys. Lett.* **89**, 483 (1982).
- [35] T. N. Rescigno and C. W. McCurdy, *Phys. Rev. A* **62**, 032706 (2000).
- [36] D. Manolopoulos and R. Wyatt, *Chem. Phys. Lett.* **152**, 23 (1988).
- [37] J. P. Burke, Jr., Ph.D. thesis, University of Colorado, Boulder, 1999.
- [38] R. A. Aziz and M. J. Slaman, *J. Chem. Phys.* **94**, 8047 (1991).
- [39] J. C. Xie, S. K. Mishra, T. Kar, and R.-H. Xie, *Chem. Phys. Lett.* **605-606**, 137 (2014).
- [40] A. M. Gardner, R. J. Plowright, M. J. Watkins, T. G. Wright, and W. H. Breckenridge, *J. Chem. Phys.* **132**, 184301 (2010).
- [41] B. D. Esry, C. H. Greene, and H. Suno, *Phys. Rev. A* **65**, 010705(R) (2001).
- [42] S. Haze, J. P. D’Incao, D. Dorer, J. Li, M. Deiß, E. Tiemann, P. S. Julienne, and J. H. Denschlag, *Phys. Rev. Res.* **5**, 013161 (2023).